2D FRETTING WEAR ANALYSIS OF MOORING CONNECTORS UNDER PLASTIC STRAIN

Matheus Zegatti

Thiago Doca

matheuszegatti@gmail.com

doca@unb.br

University of Brasília

Campus Universitário Darcy Ribeiro, 70910-900, Brasília, DF, Brasil

Abstract. *Wear is a failure mechanism that takes place on the contact interface of solids in relative motion. For instance, in the oil & gas industry wear can be observed on chain links and connectors of the mooring system. In this work, we analyze two standard mooring connectors which are modeled as elasto-plastic solids. Numerical simulations of a gross slip regime yielding plastic strains and wear are carried out on Abaqus. A Python subroutine is implemented for the optimal discretization of the contact surface. The objective of this analysis is to identify how relevant is the wear phenomena on the failure of the mooring system of offshore platforms on ultra-deep sea locations. The methods employed for the evaluation of the wear volume are the Archard method and the Dissipated energy method. The results show that the development of plastic strain on the contact surface of the mooring connectors acts as a catalyst of the fretting wear process.*

Keywords: *Contact Mechanics, Plastic Strain, Fretting Wear, FEM*

1. INTRODUCTION

Fretting wear of solid bodies in contact are observed in a vast array of mechanical applications such as overhead electrical cables, aircraft turbine blades and mooring connectors of offshore platforms.

According to Stachowiak and Batchelor (2014), fretting wear is present in contact bodies that experience small amplitude displacements (micrometer scale) over a significant number of cycles, leading to two forms of damage: surface wear and deterioration of fatigue life. In oil & gas applications, the fretting wear in conjunction with other failure mechanisms is causing premature failures. A recent review of the failures on mooring systems is presented by Ma (2013). It shows that in a period of ten years (2001-2011) several incidents were observed, where wear was a crucial factor.

The two most commonly used mooring connectors are the Marine shackle and the Kenter, see Fig. 1. The contact interface present in these two types of connectors are the cylinder in inner cylinder configuration, where the connector has a "negative radius", and the cylinder on flat plate configuration. Additional information about these components is presented in Section 2.
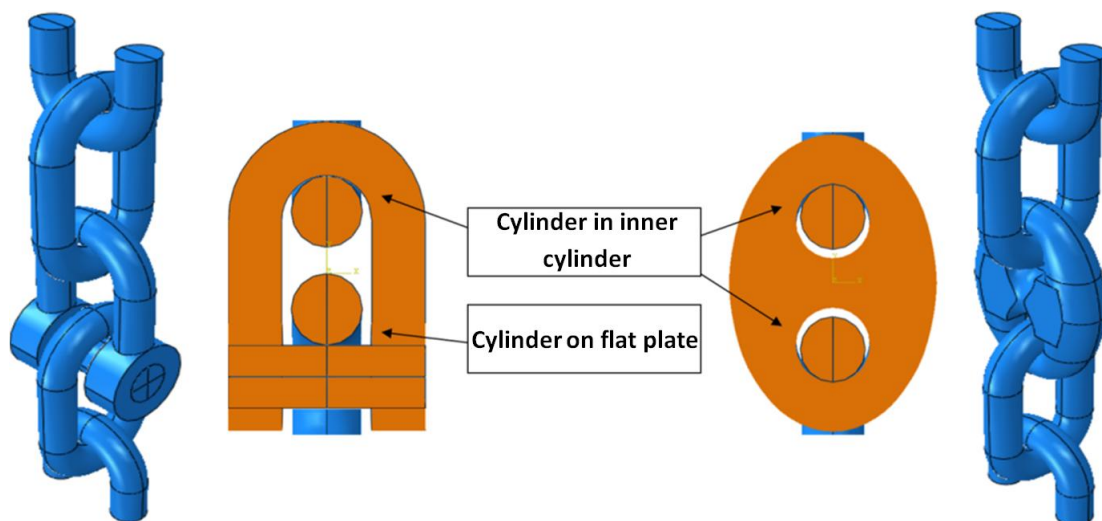

Figure 1. Connectors and contact configurations present on a mooring system. Left side: Marine shackle; Right side: Kenter

The aim of this work is to evaluate the wear volume of mooring connectors under a plastic strain regime. This analysis is conducted in three phases. First, a load is applied onto a non-Hertzian contact problem, considering that, small deformation domain, frictionless surfaces and only elastic deformations are no longer maintained (Johnson, 1985). Afterward, for a prescribed lateral displacement of the upper body, keeping the load applied previously. Finally, the global wear volume of both configurations is determined through two wear models: Archard and Dissipated energy.

CILAMCE 2016

Proceedings of the XXXVII Iberian Latin-American Congress on Computational Methods in Engineering
Suzana Moreira Ávila (Editor), ABMEC, Brasília, DF, Brazil, November 6-9, 2016

2. BACKGROUND

This work is a computational mechanics analysis (Wriggers, 2006) considering three different aspects of the contact phenomena: i) normal contact; ii) frictional/tangential contact; and iii) fretting wear. For the normal contact model, the Hertz formulation (Hertz, 1822) is employed with the sole purpose of validate the numerical results obtained below the elastic limit. For the wear estimation two approaches were employed: Archard's wear law (Archard, 1953) and the Dissipated energy model (Qiu, 1991; Rodkiewicz, 1994; Fouvry, 1996).

2.1 Hertz formulation

In order to validate at least the FEM numerical results under the elastic limit, Hertzian equations provide analytical results for the two contact configurations, cylinder in inner cylinder and cylinder on flat plate. These equations yield parameters as the contact pressure distribution, $p(x)$, the maximum contact pressure, p_0, and the contact half-width, a.

As the simulation takes place in a bi-dimensional environment, the contact is defined in a plane strain state. The contact pressure distribution is given by Eq. (1) (Hills and Nowell, 1994).

$$p(x) = p_0 \sqrt{1 - \left(\frac{x}{a}\right)^2} \tag{1}$$

Maximum contact pressure is directly proportional to the load applied in the upper body and inversely proportional to the contact half-width, as shown in Eq. (2).

$$p_0 = \frac{2P}{\pi a} \tag{2}$$

The contact half-width is given by Eq. (3), where R_{eq} is the equivalent radius, given by Eq. (4), and E_{eq} is the equivalent modulus of elasticity, given by Eq. (5). In the cylinder on flat plate configuration the flat plate radius is considered infinite, so the equivalent radius will be the same as the upper cylinder radius.

$$a = \sqrt{\frac{4PR_{eq}}{\pi E_{eq}}} \tag{3}$$

$$R_{eq} = \left(\frac{1}{R_1} + \frac{1}{R_2}\right)^{-1} \tag{4}$$

$$E_{eq} = \left(\frac{1-v_1^2}{E_1} + \frac{1-v_2^2}{E_2} \right)^{-1} \tag{5}$$

The parameters R_1, E_1, v_1, R_2, E_2, v_2 are respectively the radius, elastic modulus and Poisson's ratios of the upper (1) and bottom (2) contact bodies.

As mentioned in the beginning of this section, this formulation is important to validate the numerical conditions employed in the FEM simulation. Assuring that the numerical results below the elastic limit are similar to the analytical results presented above, the contact formulations, boundary conditions and other conditions can be carried forth in a non-Hertzian simulation, for instance in an elasto-plastic analysis. This comparison, as well as a comparison of the Muskhelishvili potential (Muskhelishvili, 1953; Gladwell, 1980; Hills et al, 1993) for analytical and numerical results, can be found in Zegatti and Doca (2016).

2.2   Wear volume estimation

Archard's wear law (1953) is a widely used method for the wear volume estimation, as can be seen in the works carried out by McColl et al. (2004), Madge et al. (2007), Cruzado et al. (2012), Bortoleto et al. (2013) and references therein. Archard states that the global wear volume, V, is expressed as a function of the normal load, P, the sliding distance, s, the material's Hardness, H, and the dimensionless wear coefficient, K. The dimensionless wear coefficient and Hardness can be replaced by a specific wear rate, k, as shown in Eq. (6).

$$V = \frac{K}{H} Ps = kPs \tag{6}$$

An alternative way to evaluate the wear volume is to quantify the energy lost due to friction, see Qiu et al. (1991), Rodkiewicz et al. (1994) and Fouvry et al. (1996). This method relates the accumulated friction energy dissipated in the interface (Ed), to the global wear volume, V, using an independent material parameter known as energy wear volume coefficient, α. This approach takes into account the effect of frictional forces.

$$V = \alpha \sum Ed \tag{7}$$

The energy dissipated is obtained from the fretting cycle, as can be seen in Fig. 2 (Garcin et al., 2015), and is given by Eq. (8).

$$Ed = \int_0^t F_t ds \tag{8}$$

In order to estimate the area produced by the energy dissipated in this fretting cycle, an approach considering the friction force constant is employed. This dissipated energy is evaluated taking the average friction force, $F_{t,avg}$, over the sliding, s.
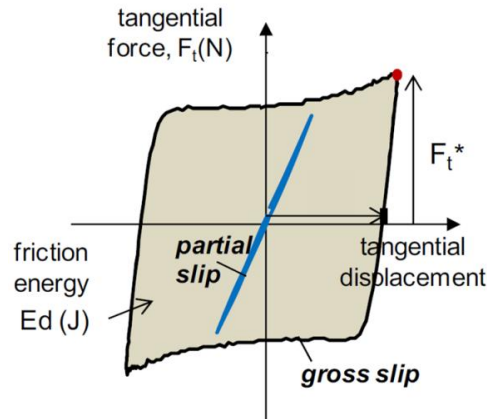
$$Ed = F_{t,avg}\, s \tag{9}$$

Figure 2. Friction energy dissipated obtained for two sliding regimes

Moreover, the energy dissipated is represented by the area bellow the frictional force curve. Therefore, the wear volume of the Dissipated energy model can be obtained by Eq. (10).

$$V = \alpha F_{t,avg}\, s \tag{10}$$

3.   PROBLEM DESCRIPTION

This section describes the aspects of the problem such as geometries, material properties, loads, displacement conditions, the different phases of the analysis and also particularities of the numerical model employed in the FEM simulation. The software adopted to run the numerical simulations was Abaqus Standard version 6.14®. The input files with optimized meshes of the two contact configurations were developed in Python®.

3.1   Geometries and material properties

The two contact configurations, the cylinder on flat plate and the cylinder in inner cylinder, are shown in Fig. 3 along with their dimensions (mm). Table 1 presents the material properties considered in the numerical model.

The material used in this analysis is the R4 grade steel, often employed in offshore mooring chains. The yield strength, tensile strength and hardening curve, shown in Tab. 1, were acquired from Bastid and Smith (2013). The Archard wear coefficient, k, and the energy wear coefficient, α, for steel can be found in Ramalho and Miranda (2006).
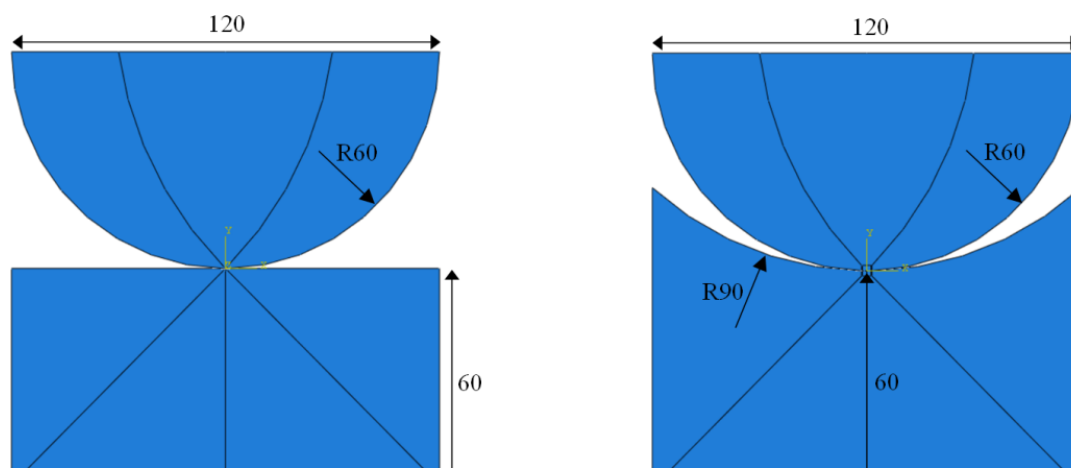
Figure 3. Dimensions of both contact pairs (given in $\boldsymbol{mm}$)

Table 1. R4 grade Steel properties

Elastic modulus	$E\ (GPa)$	210
Poisson's rate	ν	0.3
Density	$\rho\ (kg/m^3)$	7870
Coefficient of friction	μ	0.62
Yield strength	$\sigma_y\ (MPa)$	871
Hardening curve	$\sigma_u\ (MPa)/\varepsilon$	1018/0.088
(Stress / Eq. Plastic Strain)	$\sigma_u\ (MPa)/\varepsilon$	1018/0.2
Archard wear coefficient	$k\ (\mu m^2/N)$	0.07
Energy wear coefficient	$\alpha\ (\mu m^2/N)$	0.13

3.2   Loading, displacement and boundary conditions

In the first phase of the numerical simulation, a load of $-12\ kN/mm$ is applied to the higher face of the upper body of both contact pairs. In the second one, the same load is kept constant during a prescribed amplitude displacement of $600\ \mu m$, applied to a reference point connected to the upper face of the upper body. At the last phase, the wear volume is evaluated for three loading conditions $(-6\ kN/mm, -9\ kN/mm$ and $-12\ kN/mm)$ and a prescribed amplitude displacement of $600\ \mu m$. Figure 4 displays the conditions employed for the cylinder in inner cylinder case. Load and displacement conditions are summarized on Tab. 2.

Table 2. Load and displacement conditions

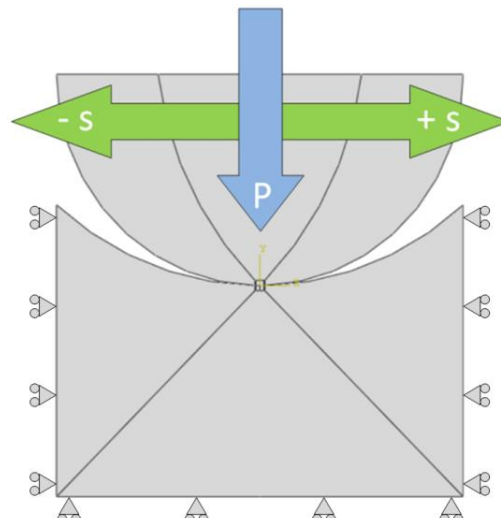| Analysis	Load, P (kN/mm)	Displacement, s (μm)
Phase I	-12	0
Phase II		600
Phase III	-6	600
	-9	
	-12	

Figure 4. Load, displacement and boundary conditions for the cylinder in inner cylinder case

3.3   Numerical model

Here, the interaction between the contacting bodies is defined as a surface-to-surface formulation with finite sliding, where the master surface belongs to the bottom body and the slave surface to the upper body. This configuration is chosen as a recommendation from Abaqus (2014) in order to reduce possible errors related to the contact results. Respectively for the normal and tangential contact constraints, the penalty and Lagrange multiplier algorithms are chosen. The penalty formulation chosen for the normal contact behavior should provide accurate results for the conditions employed. However, for the tangential contact formulation, we choose Lagrange multiplier in order to obtain more accurate results for the real sliding distance and friction force (Cruzado, 2012; Madge, 2008). Table 3 summarizes all the contact conditions selected in the numerical model.

Table 3. Proprieties of the contact formulation

Master surface	*Bottom*
Slave surface	*Upper*
Surface interaction method	*Surface-to-Surface*
Sliding formulation	*Finite sliding*
Normal contact algorithm	*Penalty*
Tangential contact algorithm	*Lagrange Multiplier*

In the step settings the non-linearity option is turned on in order to capture the effects produced by plasticity, such as large strains and rotations.

Mesh discretization is also an important factor to provide reliable results. For all contact pairs, a rectangular region ($circa\ 6a\ x\ 3a$) is symmetrically partitioned near to the contact point, willing to capture the best results for stresses, strains and contact outputs, such as contact pressure distribution and contact width. In this contact region the elements are more refined than the rest of the model. Quadrilateral linear plane strain elements with reduced

integration are chosen to this structured mesh region. Out of this contact region, the outer region is meshed freely with triangular linear plane strain elements. This mesh composition makes the simulation less computationally costly. The element applied in the first analysis has a size of $40\ \mu m$, in the other two analyses the element size has $700\ \mu m$. An illustration of the mesh composition of this later element size is displayed for the cylinder on flat plate contact pair in Fig. 5.
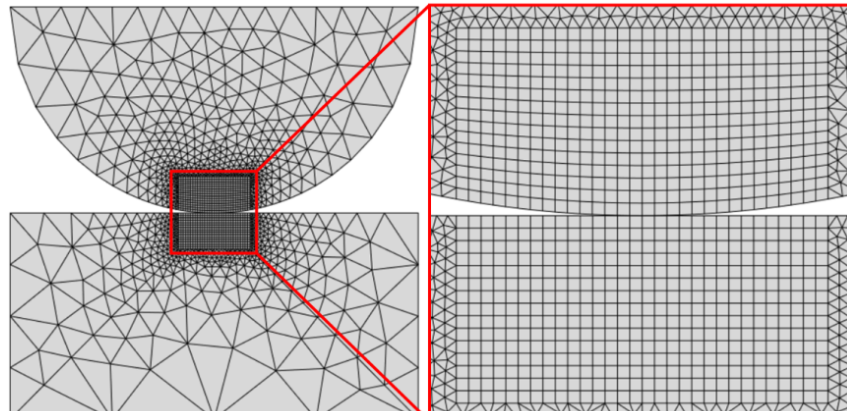

Figure 5. Mesh discretization

4. RESULT ANALYSIS

The problem studied in this work is analyzed in three phases:

1) Assessment of stresses and plastic strains produced by normal load only;

2) Assessment of stress and plastic strain fields, produced by a combination of a normal load and a prescribed displacement;

3) Assessment of the wear volume produced by three combinations of normal load and a prescribed displacement.

4.1 Phase I: Upsetting

The only load condition applied in the first phase of the analysis is the $P = -12\ kN/mm$, on the upper body. The stress fields produced by this loading, in both configurations, are shown in Fig. 6.

Initially some differences can be noticed in the stress fields outcomes. The result displayed in Fig. 6a shows a higher maximum von Mises stress value, this result is also shown on Tab. 4. Its stress field distribution differs from the elastic stress field distribution obtained in a Hertzian analysis. This happens due to the yielding of some finite elements. This event leads to an expansion of the maximum value region on the stress field, which becomes larger and also closer to the contact interface. The region that has already suffered plastic strain at this moment can be seen in the equivalent plastic strain fields of Fig. 7a.
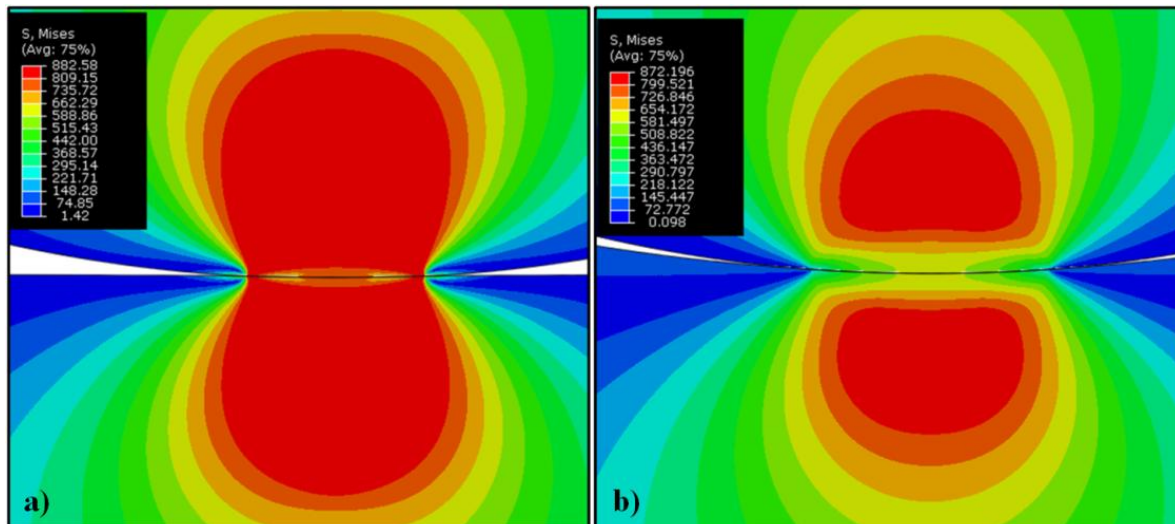
CILAMCE 2016

Proceedings of the XXXVII Iberian Latin-American Congress on Computational Methods in Engineering
Suzana Moreira Ávila (Editor), ABMEC, Brasília, DF, Brazil, November 6-9, 2016

Figure 6. Stress fields produced by a 12 kN loading. a) Cylinder on flat plate; b) Cylinder in inner cylinder

On the other hand, the stress field distribution, S_{Mises}, of the cylinder in inner cylinder (Fig. 6b) has a lower maximum value compared with the cylinder on cylinder configuration. This is a result of the geometric configuration of this contact pair. Since the contact width evolution is higher than in the other case, the load applied is distributed through a longer contact width and the stress field values reproduced are lower. In Figs. 6b and 7b we can see that the yield strength was slightly exceeded ($\sigma_y = 871\ MPa$). Because of that, the stress field distribution looks similar to an elastic one. Table 4 shows that the maximum equivalent plastic strain, $PE_{EQ,max}$, obtained is approximately ten times smaller than in the other case. In Fig. 7b the strains are at the beginning of the plastic phase. At this point, the equivalent plastic strains are far from the contact interface.
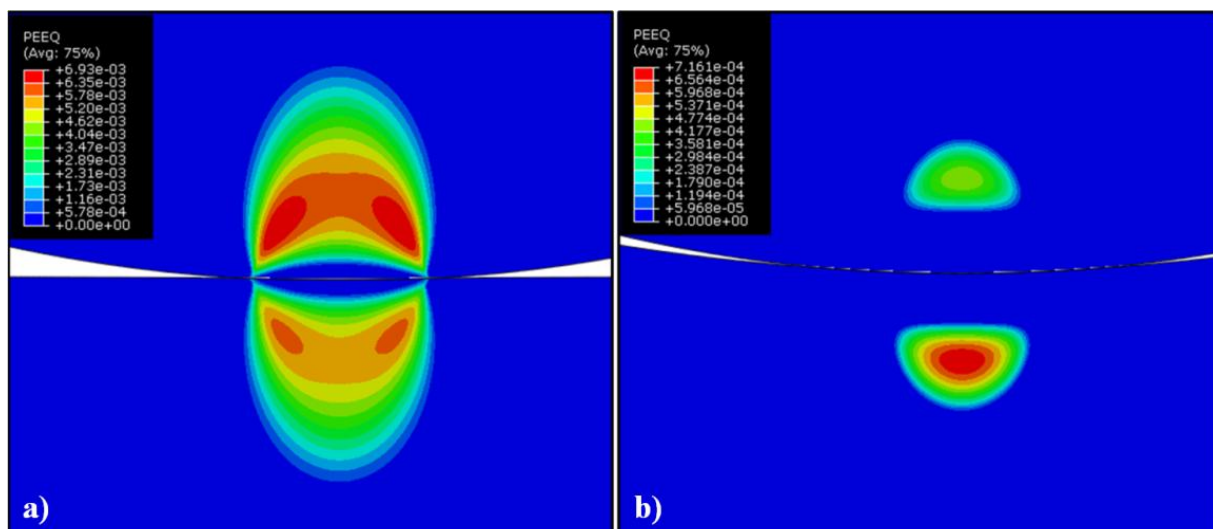

Figure 7. Equivalent plastic strain fields produced by a 12 kN loading. a) Cylinder on flat plate; b) Cylinder in inner cylinder

The behavior of the equivalent plastic strain evolution can also be analyzed. In Fig. 7b, we notice that the maximum values of the equivalent plastic strain stay initially at the center and right above the surfaces. With the evolution of the equivalent plastic strains, these values become higher at the corners of the contact surface (Fig. 7a). This can be explained by the growth of the shear stress field, S_{12}, at the contact corners, which is led by the shear contact pressure. The shear stress field of the cylinder on flat plate contact pair is presented in Fig.8.
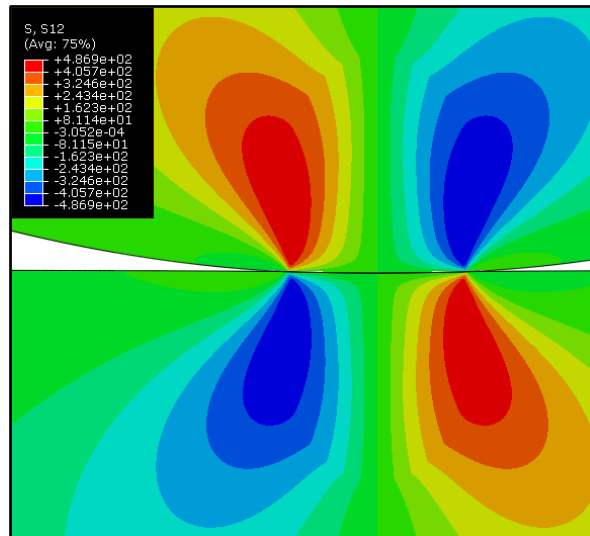

Figure 8. Cylinder on flat plate shear stress field produced by a 12 kN/mm loading

Table 4. Maximum stress and equivalent plastic strain of both contact pairs

Contact Pair	$S_{Mises,max}$ (MPa)	$S_{12,max}$ (MPa)	$PE_{EQ,max}$
Cylinder on flat plate	882.58	486.87	6.93 10^{-3}
Cylinder in inner cylinder	872.20	390.59	7.16 10^{-4}

The contact pressure distribution, shown in Fig. 9, is another interesting parameter to discuss. A comparison between the values obtained for this elasto-plastic simulation and values obtained for an Hertzian analytical formulation (Section 2.1) is made to evidentiate the elasto-plastic effects displayed in the contact pressure distributions and contact widths.
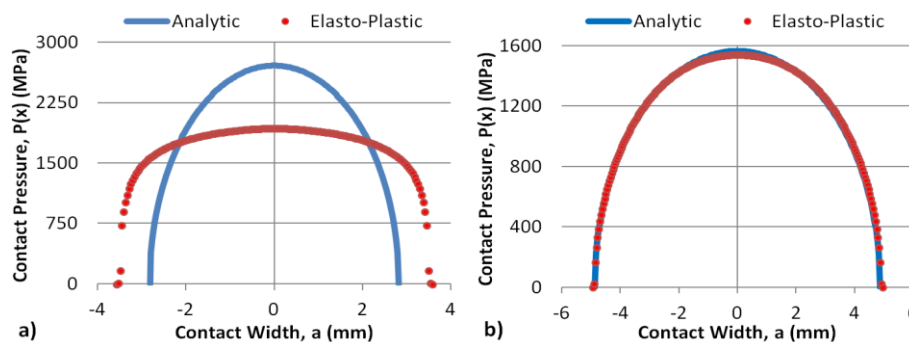

Figure 9. Comparison between the analytical elastic solution and the elasto-plastic simulation. a) Cylinder on flat plate; b) Cylinder in inner cylinder

CILAMCE 2016

Proceedings of the XXXVII Iberian Latin-American Congress on Computational Methods in Engineering
Suzana Moreira Ávila (Editor), ABMEC, Brasília, DF, Brazil, November 6-9, 2016

The cylinder in inner cylinder configuration (Fig. 9b) presents very similar results between the elasto-plastic simulation being handled and the analytical elastic results. As discussed above and shown by Fig. 6b and 7b, only a small equivalent plastic strain was observed. Because of that, the results obtained are very similar.

On the other hand, in the cylinder on flat plate contact pair, a greater equivalent plastic strain field is experienced. The chart of Fig. 9a also reproduces this effect clearly. With a significant hardening of both bodies, the maximum contact pressure becomes lower and the contact width increases. It is also noticed that the contact pressure gradient becomes smoother in the middle and rougher at the corners of the contact. The values of the contact half-width and maximum contact pressure for both simulations are given in Tab. 5, where $P_{0,ana}$, a_{ana}, $P_{0,pla}$ and a_{pla} are respectively, the maximum contact pressure and contact half-width for the analytical elastic formulation and for the elasto-plastic model.

Table 5. Contact half-width and maximum contact pressure of an analytical elastic formulation and an elasto-plastic model

Contact Pair	$P_{0,ela}\ (MPa)$	$P_{0,pla}(MPa)$	$a_{ela}\ (mm)$	$a_{pla}(mm)$
Cylinder on flat plate	2710.3	1934.7	2.8187	3.5777
Cylinder in inner cylinder	1564.8	1541.6	4.8821	4.9478

4.2   Phase II: Gross slip regime

In this second phase of the analysis, a normal load of $-12\ kN/mm$ is kept constant and a prescribed displacement of $600\ \mu m$ is introduced. The normal load and displacement values over the time, are displayed by Fig. 10. Stress and strain fields are captured 2 times during the fretting cycle, at the central points 2 and 4, which are located at the same place as the initial position, point 0. Points 1 and 3 are the most extreme right and left positions of amplitude displacement imposed to the upper cylinder, respectively.
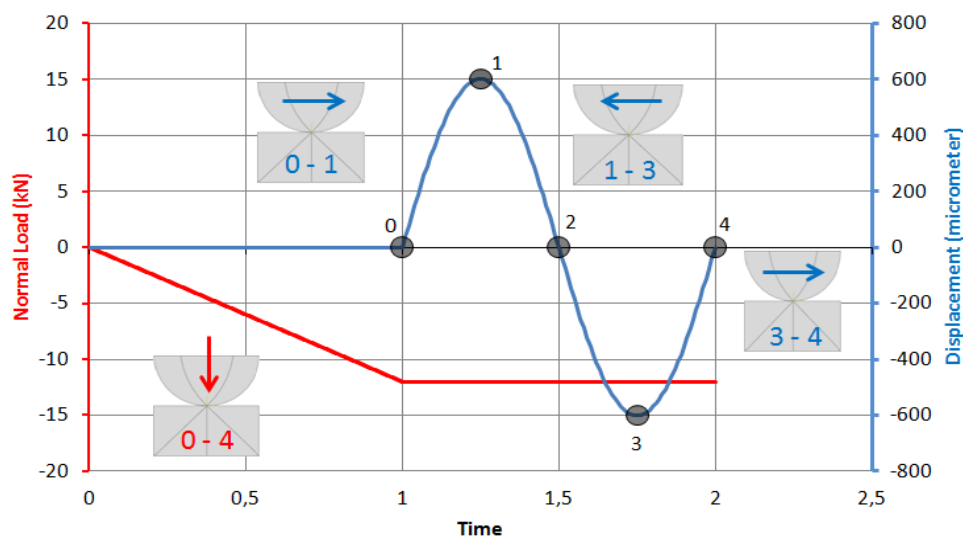

Figure 10. Load and displacement conditions imposed to the upper cylinders

The cylinder on flat plate and the cylinder in inner cylinder stress and equivalent plastic strain fields are shown in Fig. 11 and 12, respectively.
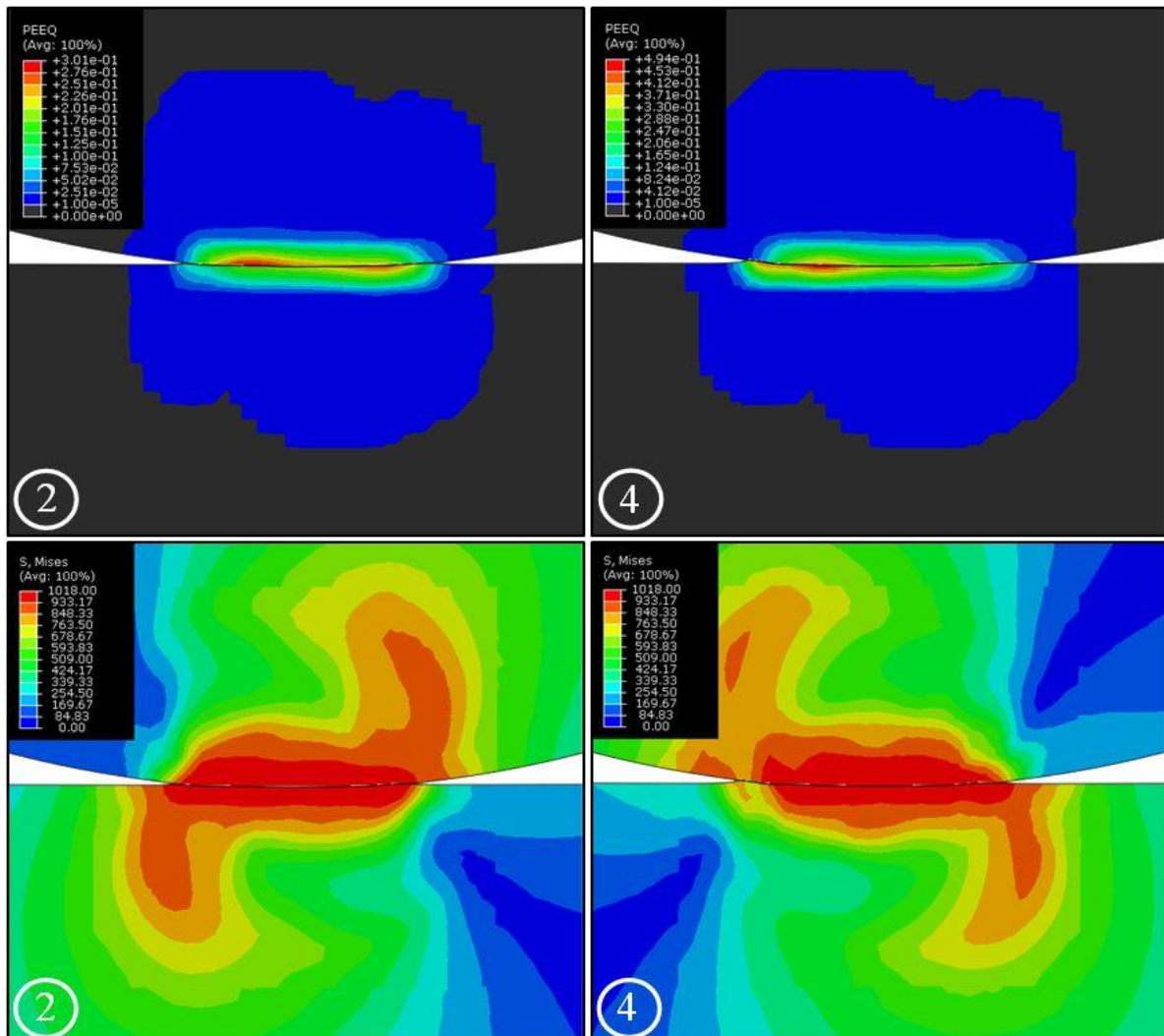

Figure 11. Cylinder on flat plate stress (down) and equivalent plastic strain fields (up) at points 2/4

Differently from the loading phase, the maximum von Mises stress remains now at the contact interface. The maximum possible stress value is reached rapidly in the displacement step, it can be observed already for the point 1 of both cases, as shown in Tab. 6. The shape of the stress field is highly influenced by the friction force between the bodies, giving an inverse mirror format for one body to another. From point 2 to point 4 an inversion of the stress field is noticed due to the displacement direction reversal. Nevertheless, the shape and value of the stress field doesn't change significantly from point 2 to point 4, except for the inversion commented above. The same can't be said for the equivalent plastic strain fields also displayed in Fig. 11 and 12.

The shape remains almost the same, but the equivalent plastic strains growth constantly with the upper body movement. The maximum equivalent plastic strain values, for each step highlighted in Fig. 10, can be consulted in Tab. 6. Something interesting is observed, the maximum equivalent plastic strain of the cylinder on flat plate is higher at the first point, but

CILAMCE 2016

Proceedings of the XXXVII Iberian Latin-American Congress on Computational Methods in Engineering
Suzana Moreira Ávila (Editor), ABMEC, Brasília, DF, Brazil, November 6-9, 2016

as soon as more displacement is introduced, this value becomes higher for the cylinder in inner cylinder contact pair. This happens because while more displacement is applied, the larger geometrical restriction of the cylinder in inner cylinder configuration becomes a relevant factor for the equivalent plastic strain evolution.
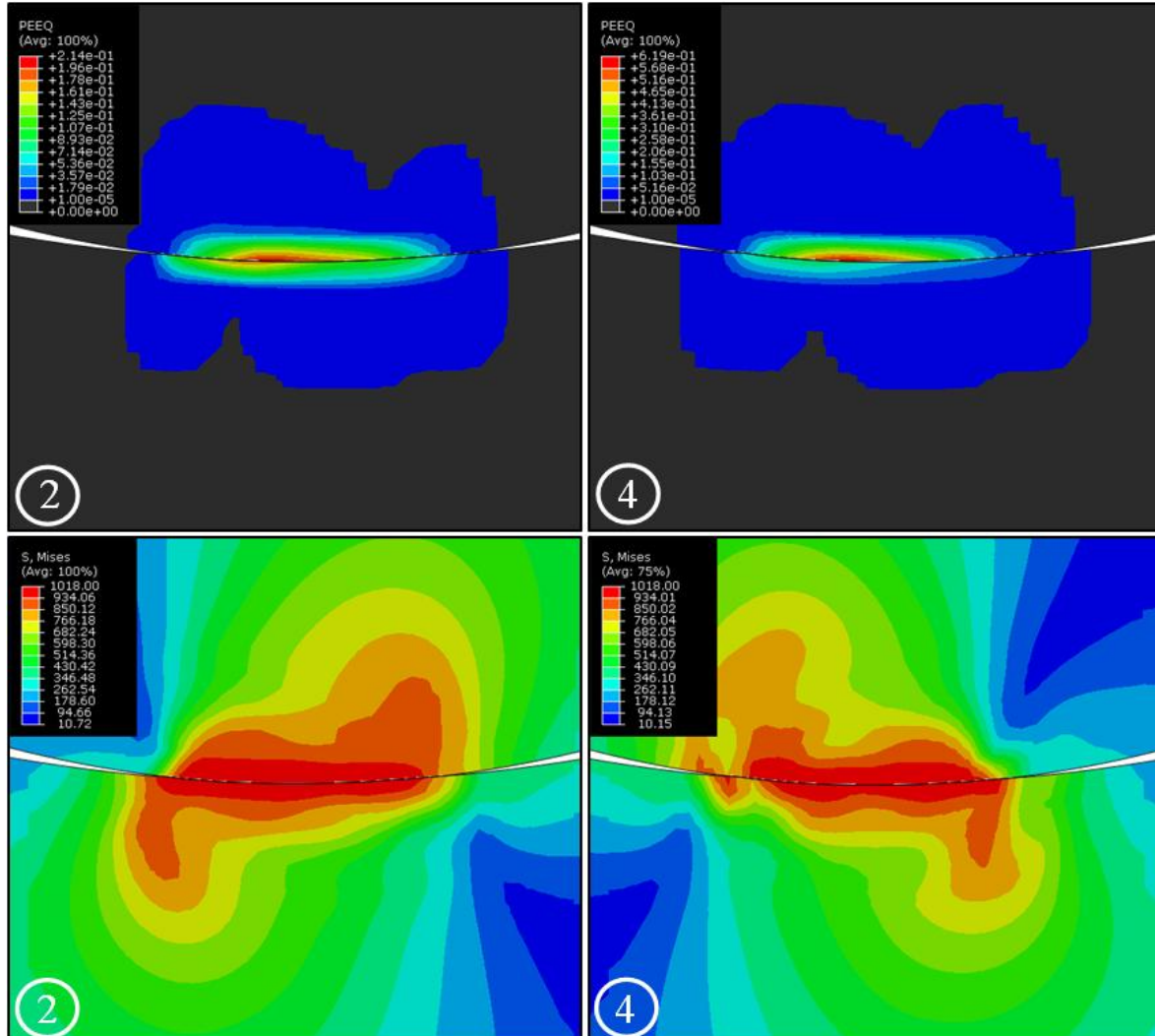

Figure 12. Cylinder in inner cylinder stress (down) and equivalent plastic strain fields (up) at points 2/4

Table 6. Cylinder on flat plate stress and equivalent plastic strain maximum at points 2/4

Point	Cylinder on flat plate		Cylinder in inner cylinder	
	$S_{Mises,max}$ (MPa)	$PE_{EQ,max}$	$S_{Mises,max}$ (MPa)	$PE_{EQ,max}$
1	1018	0.257	1018	0.204
2	1018	0.301	1018	0.214
3	1018	0.482	1018	0.524
4	1018	0.494	1018	0.619

4.3   Phase III: Fretting wear

For the estimation of the wear volume using the Archard's wear law, only the Archard's wear coefficient, the load applied and the real sliding distance are needed. The first two parameters are already known. To define the real sliding distance, the displacement of the central points of the master and slave contact surfaces, at a stabilized cycle, are used. The diagrams presented in Fig. 13 and 14, show these displacements and also the prescribed displacement at the reference point (displacement employed: $600 \ \mu m$) over the time. Figure 13 presents the results for the cylinder on flat plate configuration, with a load of $-12 \ kN/mm$, and Fig. 14 presents the results for the cylinder in inner cylinder configuration with a load of $-6 \ kN/mm$.
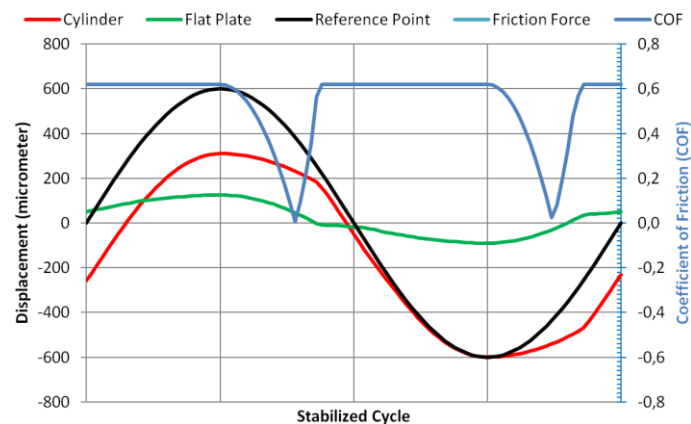

Figure 13. Displacement and coefficient of friction curves for the cylinder on flat plate configuration
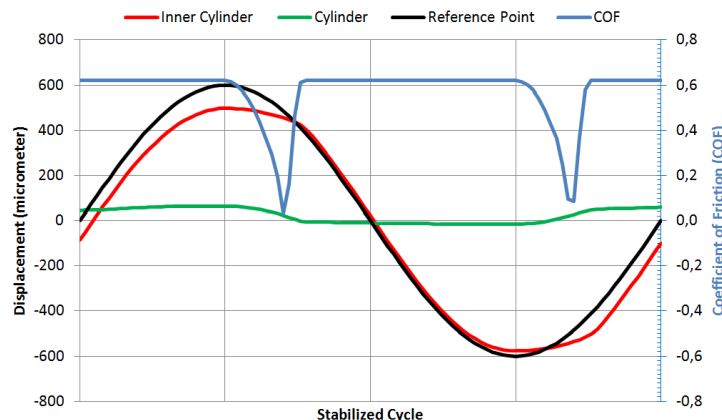

Figure 14. Displacement and coefficient of friction curves for the cylinder in inner cylinder configuration

These specific configurations were chosen because they show contrasting sliding conditions. For instance, in the cylinder on flat plate configuration the relative displacement between the bodies is smaller than in the cylinder in inner cylinder configuration shown in Fig. 14. It can also be noticed from Fig. 13 that the upper body reaches longer distances and the bottom body reaches smaller distances compared with the contact pair of Fig. 14. Another factor that shows this sliding distance difference is the period without sliding. When the

sliding direction is changed, some period without sliding is experienced. These periods appear right after the first and third quarters of the stabilized cycle and they can be observed looking at the coefficient of friction curve. For the cylinder on flat plate, the periods are longer than the periods of the cylinder in inner cylinder configuration. This happens due to the higher tangential force in this case, which makes the sliding more difficult. The average tangential forces for each case are given in Tab. 7. All these factors together produce distinct sliding distances for each contact pair under different loading conditions. Table 8 shows the relative displacement of both contact pairs for each load employed. It can be seen for the two contact pairs that as the load increases the sliding distance decreases, but this decrease is more sharp for the cylinder in inner cylinder case.

Table 7. Average friction force for each contact pairs in three loadings

Load	Average friction force, $F_{t,avg}$ (N/mm)	
(kN/mm)	Cylinder on flat plate	Cylinder in inner cylinder
−6	3725.48	3736.06
−9	5648.34	5648.34
−12	7564.43	7579.36

Table 8. Relative displacement of the contact pairs for three loadings

Load	Real sliding distance, s (μm)	
(kN/mm)	Cylinder on flat plate	Cylinder in inner cylinder
−6	1934.09	1954.46
−9	1755.52	1360.70
−12	1416.26	687.42

After the determination of the relative displacements and the average friction force, the wear volume can be estimated for the two models using Eq. (6) and (10). A thickness of 1 mm of the contact pair is considered to estimate the wear volume. The values obtained for the Archard's and the Dissipated energy models are given in Tab. 9 and 10.

Table 9. Wear volume estimated by the Archard's model

Load	Archard wear volume (mm^3)	
(kN/mm)	Cylinder on flat plate	Cylinder in inner cylinder
−6	$0.812.10^{-3}$	$0.821.10^{-3}$
−9	$1.106.10^{-3}$	$0.857.10^{-3}$
−12	$1.190.10^{-3}$	$0.642.10^{-3}$

Table 10. Wear volume estimated by the Dissipated energy model

Load	Dissipated energy wear volume (mm^3)	
(kN/mm)	Cylinder on flat plate	Cylinder in inner cylinder
−6	$0.936.10^{-3}$	$0.949.10^{-3}$
−9	$1.289.10^{-3}$	$0.999.10^{-3}$
−12	$1.392.10^{-3}$	$0.753.10^{-3}$

For the two contact pairs of both wear models, the largest wear volumes were verified in cases where higher normal loads were applied, except for the case of the cylinder in inner cylinder with a load of $-12 \, kN/mm$. In this case, the larger wear area produced by the higher normal load is not sufficient to give a larger wear volume, this happens because the sliding distance is much smaller compared to the others sliding distances of the cylinder in inner cylinder configuration. For all the other cases an increase in the wear volume was noticed as the load increases. In the cylinder on flat plate this outcome was more clear since the sliding distances don't differ widely. Looking at the results on Tab. 9 and 10, the Dissipated energy model yields larger wear volumes for all cases in comparison to the Archard's model. For that reason, it can be said that the Dissipated energy model, in this analysis, showed to be more conservative.

5.   CONCLUSIONS

This work presented the result of a 2D frictional contact analysis executed in three different phases. In the first one, results for the same loading applied in the two contact pairs show that higher equivalent plastic strains are observed in the cylinder on flat plate configuration through a larger region. This happens because in the cylinder in inner cylinder contact pair, the load is distributed through a longer contact width, and as a consequence, the stress field observed presents lower values. For this load, many elements of the cylinder in inner cylinder do not reach the yield strength, displaying very similar results of an Hertzian analysis. On the other hand, the cylinder on flat plate results showed that the maximum contact pressure, contact half-width and the stress field change significantly when compared to an elastic Hertzian analysis.

The second analysis presented the stress and strain fields for both configurations in a prescribed lateral displacement with a normal load applied at the upper body. The results show that the plastic strains observed in this phase are higher than the ones observed in the first phase and remain at the contact pair surfaces. This is a consequence of the friction force acting at the surfaces. The tensile strength is reached in the early steps of the displacement at the surfaces, yielding higher plastic strains. The highest plastic strain was observed for the cylinder in inner cylinder case, due to the geometrical configuration that imposes higher restriction to the movement.

The fretting wear analysis presents the estimation of the wear volume based on two methods. For both methods and for the two contact pairs, as the normal load increases the wear volume also increases, except for one case where the measured sliding distance was much smaller diminished. However, the increase on the wear volume due to the higher normal loads create a larger adhesion zone inside the contact interface which mitigates the evolution of the wear phenomena. Comparing the two models, the Dissipated energy model yielded more conservative results, considering that for all the cases studied the wear volume was larger on this model.

CILAMCE 2016

Proceedings of the XXXVII Iberian Latin-American Congress on Computational Methods in Engineering
Suzana Moreira Ávila (Editor), ABMEC, Brasília, DF, Brazil, November 6-9, 2016

ACKNOWLEDGEMENTS

REFERENCES

Abaqus 6.14, 2014. Benchmarks Manual, Dassault Systèmes.

Archard, J.F., 1953. Contact and rubbing of flat surfaces, Journal of Applied Physics 24, 981–988.

Bastid, P., Smith, S.D., 2013. Numerical analysis of contact stresses between mooring chain links and potential consequences for fatigue damage. ASME 55331, Volume 2B, OMAE2013-11360.

Bortoleto, E.M., et al., 2013. Experimental and numerical analysis of dry contact in the pin on disc test. Wear (Lausanne), v. 301, p. 19-26.

Cruzado A., Urchegui M.A., Gómez X., 2012. Finite element modeling and experimental validation of fretting wear scars in thin steel wires. Wear; 289:26–38.

Fouvry, S., Kapsa, Ph., Vincent, L., 1996. Quantification of fretting damage. Wear 200 186-205.

Garcin, S., Fouvry, S., Heredia, S., 2015. A FEM fretting map modeling: Effect of surface wear on crack nucleation, WEAR, 330-331, 145-159.

Hertz, H., 1882. Über die Berührung fester elastischer Körper. Jnl Reine und angewandte Mathematik, 92, pp. 156-171.

Hills, D. A. e Nowell, D., 1994. Mechanics of Fretting Fatigue, Solid Mechanics and its Applications. Kluwer Academic Publishers, Oxford, Reino Unido.

Hills, D. A., Nowell, D., Sackfield, A., 1993. Mechanics of Elastic Contacts. Butterworth-Heinemann, Oxford.

Johnson, K. L., 1985. Contact Mechanics. Cambridge University Press, 452p.

Ma, K.T. et al., 2013. A historical review on integrity issues of permanent mooring systems. Offshore technology conference 2013-24025.

Madge J.J., Leen S.B., McColl I.R., Shipway P.H., 2007. Contact-evolution based prediction of fretting fatigue life: Effect of slip amplitude. Wear; 262(9–10):1159–70.

Madge, J.J., Leen S.B., Shipway P.H., 2008. A combined wear and crack nucleation-propagation methodology for fretting fatigue prediction. International Journal of Fatigue.

McColl , I.R., Ding, J., Leen, S.B., 2004. Finite element simulation and experimental validation of fretting wear. Wear 256 1114–1127.

Muskhelishvili, N. I., 1953. Some basic problems of mathematical theory of elasticity. Noordhoff, Groningen, 36, pp. 99-107.

Qiu, X., Plesha, M.E., 1991. A theory for dry wear based on energy. Trans. ASME, J. Tribal., III 442-451.

Ramalho, A., Miranda, J.C., 2006. The relation between wear and dissipated energy in sliding systems. Wear, 260, 361-367.

Rodkiewicz, C.M., Wang, Y., 1994. A dry wear model based on energy consideration. Tribal. Int., .27 145-151.

Stachowiak, G.W., Batchelor, A.W., 2013. Engineering Tribology (Fourth Edition), Butterworth-Heinemann, Elsevier Science & Technology Books.

Wriggers, P. 2006. Computational Contact Mechanics (Second Edition), Springer-Verlag, Berlin Heidelberg.

Zegatti, M., Doca, T., 2016. Estudo numérico e analítico de problemas de contato hertziano. XII Simpósio de mecânica computacional, 516-523.

CILAMCE 2016

Proceedings of the XXXVII Iberian Latin-American Congress on Computational Methods in Engineering
Suzana Moreira Ávila (Editor), ABMEC, Brasília, DF, Brazil, November 6-9, 2016